Environmental Earth Sciences (2018) 77:183
https://doi.org/10.1007/s12665-018-7334-5

ORIGINAL ARTICLE

Object-oriented change detection and damage assessment using high-resolution remote sensing images, Tangjiao Landslide, Three Gorges Reservoir, China

Faming Huang[1,2] · Lixia Chen[2] · Kunlong Yin[2] · Jinsong Huang[3] · Lei Gui[2]

Received: 6 May 2017 / Accepted: 12 February 2018 / Published online: 27 February 2018

Abstract
This paper presents a new approach for tracking land cover changes and assessing damages caused by individual reservoir landslides using high-resolution images. The object-oriented change detection (OOCD) approach has recently become more popular than traditional pixel-oriented methods for high-resolution image analysis. However, few studies have applied the OOCD approach to the land cover change detection (LCCD) and the damage assessments of individual landslide. An OOCD approach was applied to the multi-temporal high-resolution images taken in 2002, 2005, 2010 and 2013 throughout the Tangjiao Landslide in the TGRA. The proposed OOCD approach contains three major steps: land-cover-type analysis, high-resolution image classification using an object-oriented classification method and LCCD via comparing the classified geographic objects in different temporal images. The object-oriented classification results show that the overall classification accuracies of the 2005, 2010 and 2013 images were greater than 92%, with Kappa Index of Agreement values of at least 89%. The IKONOS image taken in 2002 is an exception to both of these values. Land cover change maps suggest that various damages occurred throughout the study area from 2002 to 2013. Large woodland areas were submerged at the front of the study area. In addition, 21,365 m^2 buildings and a 300-m-long road were damaged between 2005 and 2010. Furthermore, a large surface crack was observed from 2010 to 2013. The results suggest that the OOCD approach is able to effectively and accurately identify damage characteristics on the individual landslide. The results also show that the instability of Tangjiao Landslide is controlled by the geological conditions and seriously affected by the reservoir water-level fluctuation and seasonal rainfall.

Keywords Reservoir landslide · High-resolution remote sensing images · Object-oriented change detection · Damage assessment

Introduction

Reservoir landslides are serious geological problems (Huang et al. 2017b; Lan et al. 2004). Landslides pose serious safety threats to local residents and property. These hazardous events can also destroy ecological environments. Therefore, reservoir landslides must be monitored using earth observation techniques (Huang et al. 2017a; Kirschbaum and Fukuoka 2012; Van Westen and Getahun 2003; Vijay et al. 2016).

Land cover changes are considered important landslide indicators. Damage information can be obtained via land cover change detection (LCCD) based on field investigations. However, most recent studies have focused on landslide displacement monitoring (Benoit et al. 2015; Huang et al. 2016a, b), landslide investigations (Wasowski and Bovenga 2014), hazard assessments (Fourniadis et al. 2007; Huang et al. 2017c; Metternicht et al. 2005) and inventory mapping (Fiorucci et al. 2011). Few studies have focused on LCCD for the damage assessment of individual landslides. The damage assessment of individual landslide using LCCD can reflect the damage characteristics of landslide on

✉ Kunlong Yin
yinkunlon@163.com

1 School of Civil Engineering and Architecture, Nanchang University, Nanchang 330000, China

2 China University of Geosciences, Wuhan 430074, China

3 ARC Centre of Excellence for Geotechnical Science and Engineering, University of Newcastle, Newcastle, NSW, Australia

a medium-scale level, the landslide displacement monitoring and landslide investigation analyse the landslide surface deformation on a micro-scale level, and the hazard assessments and inventory mapping study the landslide damages based on the remote sensing images in a large-scale area. Therefore, an efficient and reliable LCCD is needed for individual landslides.

Remote sensing images have become the primary data sources for LCCD. These images have advantages related to periodicity and scale. Higher-resolution images provide more detailed colour, texture and geometrical information (Kumar et al. 2006; Pacifici et al. 2009). Over the past several decades, various LCCD methods have been proposed that utilise multi-temporal remote sensing images. The post-classification comparison method (Lu et al. 2004) is one of the most common LCCD methods. In the post-classification comparison approach, the remote sensing images are first classified as either land cover maps or other thematic maps; then, the results of those classifications are then compared. The post-classification comparison approach can overcome temporal limitations, produce a deformation change information matrix and reduce the negative impacts associated with differences between images obtained from various temporal or sensory sources (Mas 1999).

The precision with which the post-classification comparison approach can detect change is largely dependent upon the accuracy of the image classification. Post-classification comparison techniques are categorised as either pixel-oriented change detection (POCD) or object-oriented change detection (OOCD) (Platt and Rapoza 2008; Walter 2004). The POCD approach provides an acceptable level of performance for moderate- and low-resolution remote sensing images (Ahlqvist 2008; Friedl et al. 2002). However, the POCD approach often produces unsatisfactory results for high-resolution images because POCD is based solely on pixel spectrum features. Therefore, this method can be improved (Gong et al. 2006). For example, the presence of different spectrums in the same object presents a serious obstacle. The land cover types within a reservoir landslide and the objects that comprise these land cover types are extremely complex. The POCD classification method may not properly determine the nature of an object. Pseudo-changes inside objects are also difficult to identify. In addition, both registration error and viewpoint changes seriously interfere with the accuracy of the POCD approach.

Compared to the traditional POCD approach, the OOCD approach provides solutions for the aforementioned problems (Duro et al. 2012; Laura and King 2011). The OOCD approach more accurately represents geographic objects. It compares image objects within different land cover maps rather than using a single pixel to counteract sensor limitations. The OOCD method can potentially produce more accurate change detection maps by incorporating neighbour properties (Blaschke and Hay 2001; Blaschke et al. 2000). In general, the OOCD approach includes three steps: original image analysis, object-oriented classification and LCCD (Chen et al. 2012). The OOCD approach has been recently applied to multiple analyses, including LCCD (Qin et al. 2013; Walker and Blaschke 2008), forest/vegetation surveying (Mallinis et al. 2008; Mathieu and Aryal 2007), damage assessment (Gusella et al. 2005; Tong et al. 2012), urban change detection (Gamanya et al. 2009) and ecological/environmental threat identification (Dronova et al. 2011; Elmqvist et al. 2008).

Landslides are widely distributed in the Three Gorges Reservoir Area (TGRA). Among these landslides, the Tangjiao Landslide is a typical reservoir landslide. The study area is within the scope of the active block of the Tangjiao Landslide. The OOCD approach was used to monitor land cover changes in the study area. Land cover change maps were created to assess the damage information.

Research area and materials

Natural geography of the Tangjiao Landslide

The Tangjiao Landslide is located in the Wanzhou District of the TGRA of China, approximately 327 km from the Three Gorges Dam. A location map is shown in Fig. 1. The Tangjiao Landslide is located within the subtropical climate belt, which receives frequent heavy rainfall events during the summer season. Tangjiao Landslide can be classified as reservoir colluvial-deposit landslide. This kind of landslides can be identified through a comprehensive process of field investigation, potential landslide inventory and surface deformation monitoring.

The water-level rise of the Three Gorges Reservoir (TGR) occurred in four phases. The original water level was approximately 70 m above sea level during the first phase. The first water-storage event occurred in June 2003, increasing the water level to 135 m. The water level fluctuated between 135 and 140 m during this second phase, which lasted from June 2003 to September 2006. The water level periodically fluctuated between 145 and 156 m during the third phase, which occurred from October 2006 to September 2008. The water level fluctuated between 145 and 175 m during the final phase, which occurred from 2009 to November 2015 (Fig. 2).

There are many landslides locating in the TGRA for all the time, because of the special geological environments, the dense river network, the seasonal rainfall induced by subtropical humid monsoon climate and the unreasonable human engineering activities (Huang et al. 2017c). However, the geological and hydrological environments of the TGRA have been affected seriously as

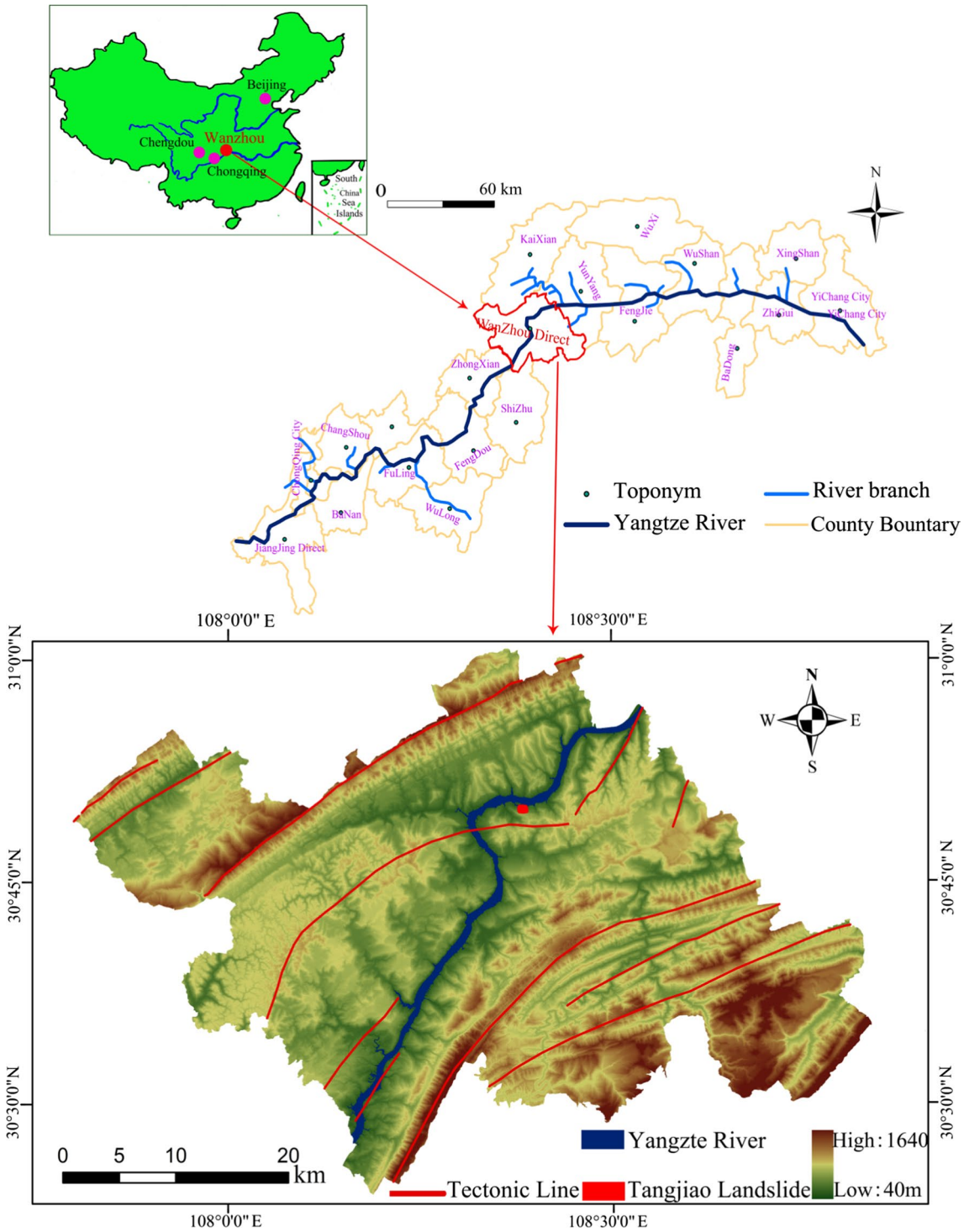

Fig. 1 Geographic location of the Tangjiao Landslide

a result of the impoundment and periodic water-level fluctuation of TGR since 2003. These effectives of TGR cause the changes in the groundwater level, in the soil physic-mechanical properties and in the land cover of the reservoir bank slopes. Due to the effectives of TGR on the reservoir bank slopes, pre-stable slopes may become landslides and ancient landslides may be activated (Huang et al. 2017b; Song et al. 2015).

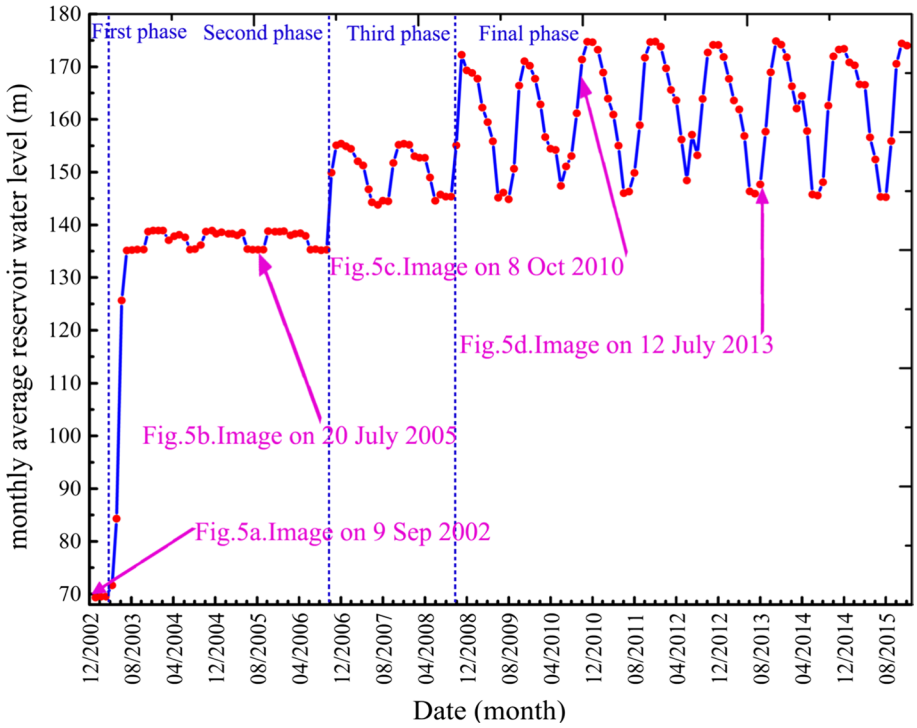

Fig. 2 Water level of TGR from 2003 to 2015

Geological conditions

The fan-shaped Tangjiao Landslide occurred on the south bank of the Yangtze River. The upper boundary of the landslide is defined by the bedrock–soil interface, which displays a chair-like shape. The maximum elevation of the upper boundary is 375 m. The left and right boundaries are both defined by seasonal gullies. The frontal part of the Tangjiao Landslide extends to the Yangtze River bed, with a toe elevation of approximately 130 m. The landslide covers an area of 125×10^4 m^2, with a longitudinal dimension of 1000 m and a width of 1250 m. The mean depth of the sliding surface is approximately 20 m. Therefore, the Tangjiao Landslide is a large accumulation landslide with an estimated volume of 2500×10^4 m^2 (Fig. 3).

The Tangjiao Landslide is divided into two main blocks according to field investigations and multi-temporal remote sensing image analyses: an active block (A) in the frontal part and a relatively stable block (B) in the middle and upper parts of the landslide. The active block exhibits serious damage and deformation characteristics as detailed in the following, while there are almost no damage areas located on the relatively block of the Tangjiao Landslide. Moreover, the active block of the Tangjiao Landslide can be considered a small reactivated landslide. Therefore, the study area within the active block is researched to assess the damage on the Tangjiao Landslide.

The Tangjiao Landslide materials are composed of medium permeable quaternary accumulations, including silty clay and fragmented rubble. The slope mass structure is loose and disordered, with a fragmented rubble content of approximately 20%. The main sliding direction is orientated towards N 354° W, with a slope of approximately 5°–25°. The bedrock lithology is mainly characterised by silty mudstones, muddy siltstones and sandstone. The dip direction is approximately 153°, and the dip angle is approximately 4° (Fig. 4).

Analysis of damage characteristics

The Tangjiao Landslide became active in 2001, when the active block exhibited local deformation and failure. Surface investigations have shown that shearing and crush-pressing cracks have occurred since the impoundment of the TGR in June 2003. A 3-m-wide concrete road located on the study area of the Tangjiao Landslide was found to have been damaged. Portions of the road also collapsed by approximately 2 m from 2002 to 2005, as shown in Fig. 7a, b.

The deformation of the study area has rapidly progressed since September 2005. Continuous deformation has completely destroyed the roads on the study area. The roads collapsed and were transported 23 m down gradient from 2005 to 2013, as shown at the macroscopic scale in Fig. 7c, d. Figure 5a illustrates the damage to the retaining wall that occurred along the road in 2008. Figure 5b shows the significant road deformation and cracking that occurred in 2011.

Since 2005, numerous buildings above the study area have been cracked, with crack widths of 3–35 cm. The

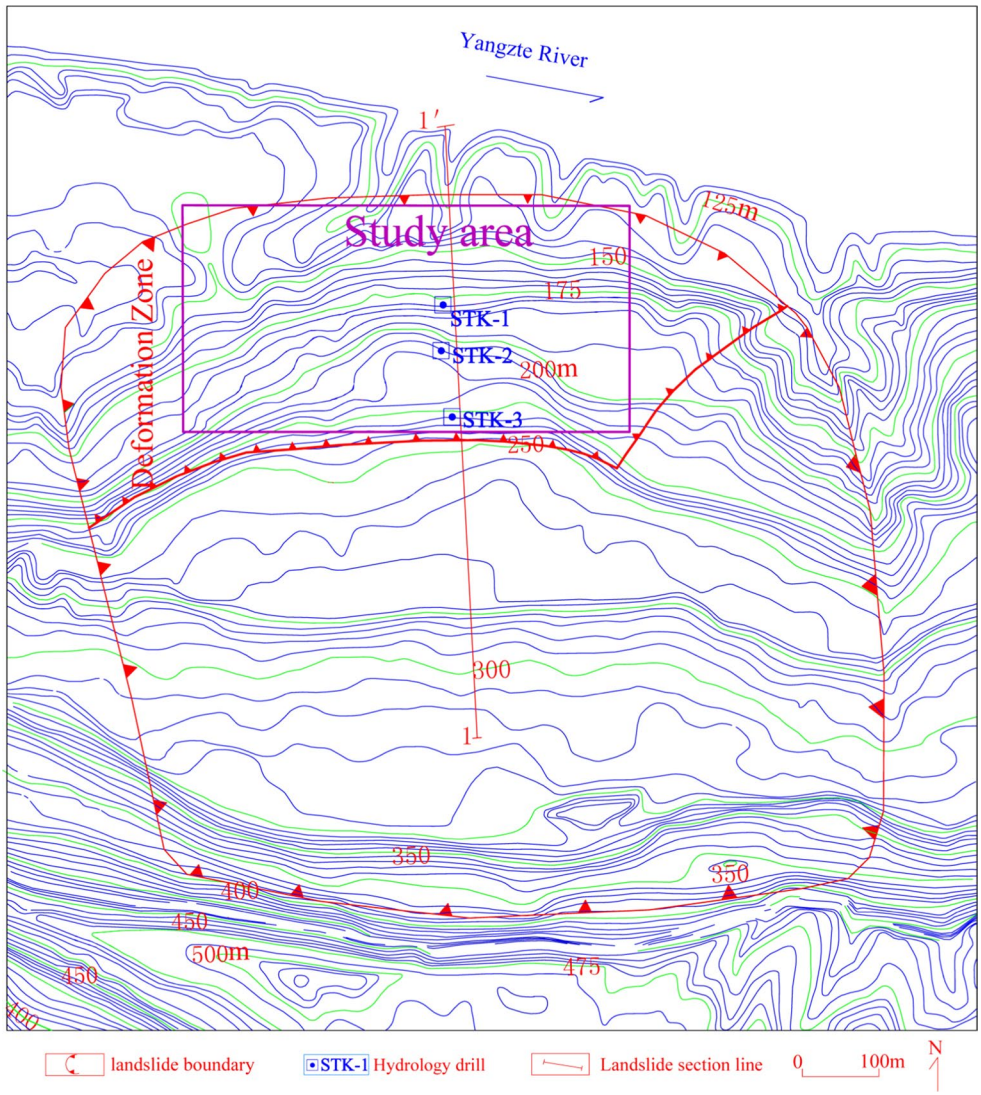

Fig. 3 Topographic map of the Tangjiao Landslide

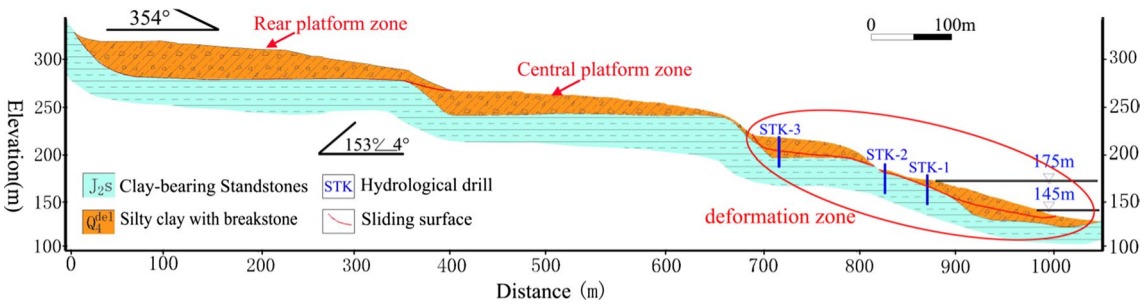

Fig. 4 Geological section of the Tangjiao Landslide

building residents have been forced to move, and buildings have been gradually dismantled. Figure 5c illustrates a tensile crack that occurred in one of the buildings. The width of the tensile crack is 53.7 mm. Figure 5d shows a large ground settlement crack that occurred in the courtyard of another building. The maximum ground settlement was approximately 85 mm, with a maximum crack width of approximately 46 mm. Numerous surface cracks and local collapses have also occurred at the study area. Figure 5e shows a surface crack that occurred under fruit trees, with a maximum

Fig. 5 Deformation and damage characteristic photographs from the study area

crack width of approximately 260 mm. Figure 5f illustrates a small debris flow that occurred in the study area after a continuous heavy rain event on 6 April 2013. Both human lives and property have been seriously threatened throughout these events. Therefore, the deformation and damage must be effectively monitored.

Multi-temporal high-resolution images

Four images were used in this study. One image was captured by the IKONOS-1 satellite on 9 September 2002. Another image was captured by the QuickBird satellite on 20 July 2005. The final two images were acquired by the WorldView-II satellite on 8 October 2010 and 12 June 2013. The details of these four high-resolution images are listed in Table 1. A visual inspection suggests that these four images are suitable for LCCD (Fig. 6). High-resolution images of the study area from 2002, 2005, 2010 and 2013 are shown in Fig. 7 Interviews with local residents were also conducted to collect land cover change information from 2000 to 2013. Manual interpretations of these four images were used to validate the LCCD results (Carlotto 2009). The detailed deformation characteristics of road and surface cracks of the study area are shown in Fig. 8.

Methods

Traditional image processing methods are mainly pixel based and incorporate little information from the image as a whole. These pixel-oriented methods often provide insufficient information. The rapid development of object-oriented classification technology has allowed for the convenient extraction of thematic information from high-resolution images.

Table 1 Band configurations of IKONOS, QuickBird and WorldView-II images

Sensor	Band numbers	Wavelengths (μm)	Acquisition date	Resolution (m)	Satellite acquisition angle (°)
IKONOS-1	3	0.45–0.52, 0.52–0.60, 0.63–0.69	9 September 2002	1	18.27
QuickBird	4	0.45–0.52, 0.52–0.60, 0.63–0.69, 0.76–0.9	20 July 2005	0.61	20.86
WorldView-II	4	0.45–0.51, 0.52–0.58, 0.63–0.69, 0.77–0.895	8 October 2010	0.5	15.51
WorldView-II	4	0.45–0.51, 0.52–0.58, 0.63–0.69, 0.77–0.895	12 June 2013	0.5	16.23

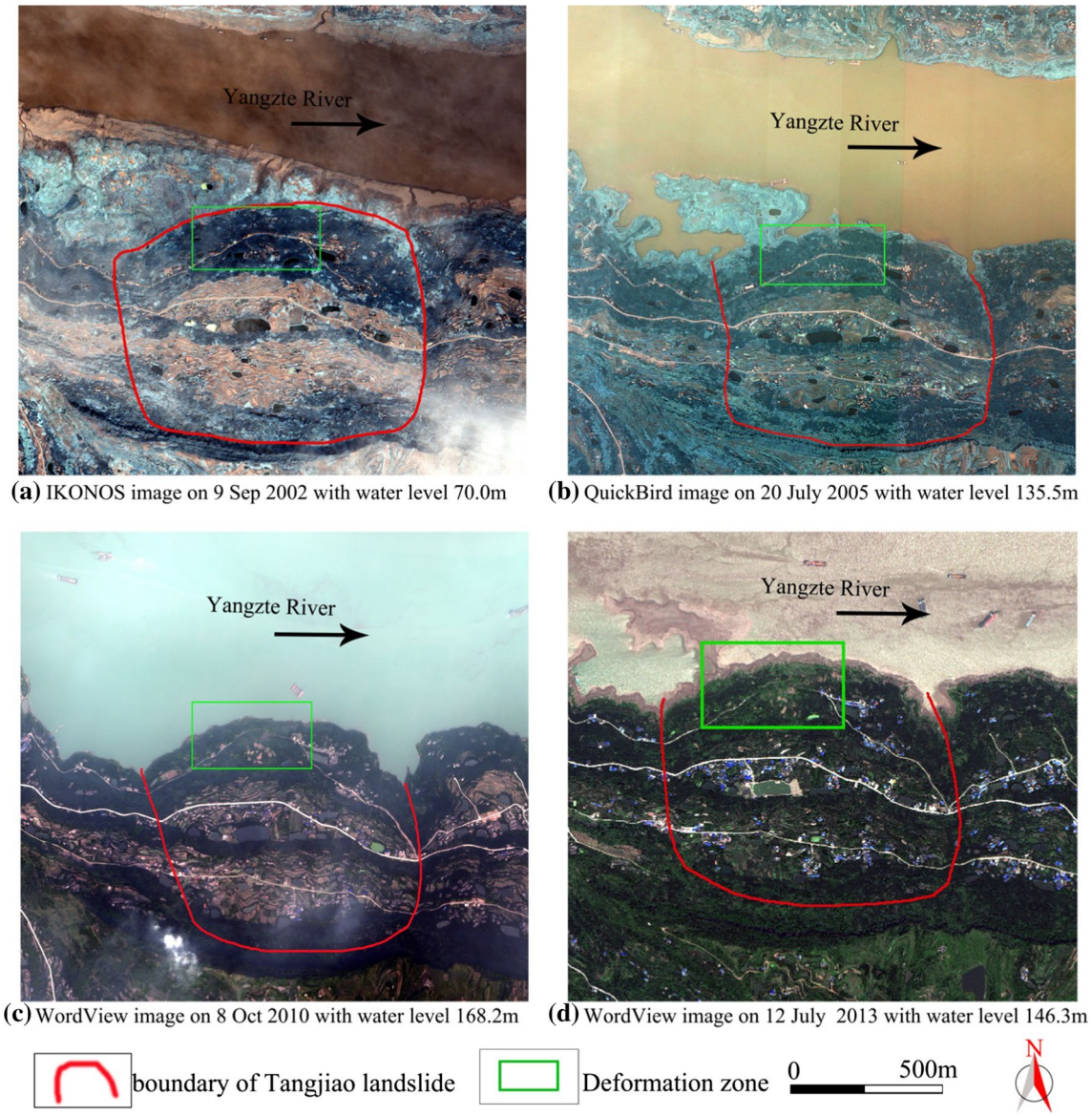

(a) IKONOS image on 9 Sep 2002 with water level 70.0m **(b)** QuickBird image on 20 July 2005 with water level 135.5m

(c) WordView image on 8 Oct 2010 with water level 168.2m **(d)** WordView image on 12 July 2013 with water level 146.3m

Fig. 6 Study site. The green rectangles outline the image locations. The red lines denote the Tangjiao Landslide boundaries

The OOCD approach proposed in this paper involves three steps. The first step analyses the land cover characteristics of multi-temporal high-resolution images based on field investigations and visual interpretations of the high-resolution images. The second step uses an object-oriented classification method to classify the high-resolution images. This method includes image segmentation,

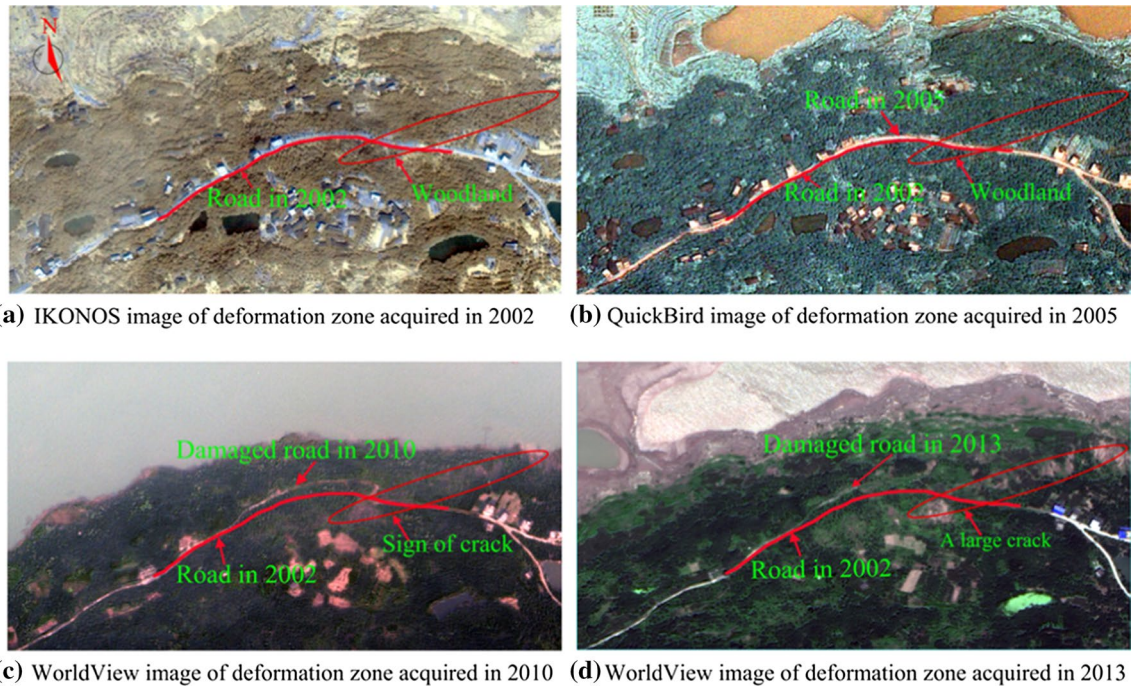

(a) IKONOS image of deformation zone acquired in 2002 **(b)** QuickBird image of deformation zone acquired in 2005

(c) WorldView image of deformation zone acquired in 2010 **(d)** WorldView image of deformation zone acquired in 2013

Fig. 7 True colour composite images (red: band 3, green: band 2, blue: band 1) of the green rectangular regions in Fig. 6

Fig. 8 Detail parts of Fig. 7

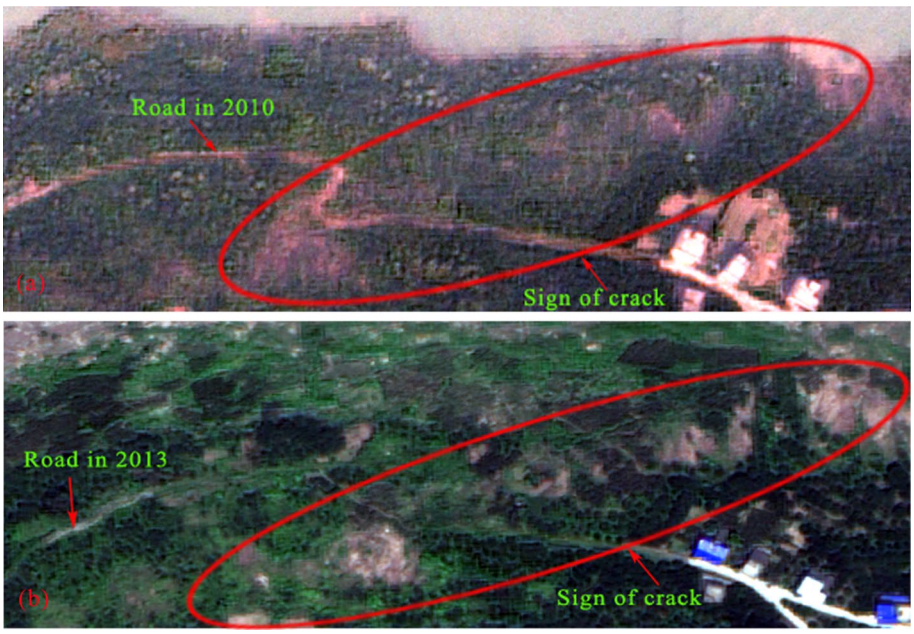

feature selection and object classification within the images. The third step involves the change detection process, which compares the classified geographic objects in different temporal images. The damage characteristics can then be assessed using LCCD. A flow chart of the proposed OOCD approach is shown in Fig. 9.

Image pre-processing

Geometric image correction based on an "image-to-image comparison" strategy was adopted to obtain accurate change detection results. The 2005 QuickBird image was chosen as the base image, while the 2002 IKONOS image and WorldView images from 2010 and 2013 were chosen as

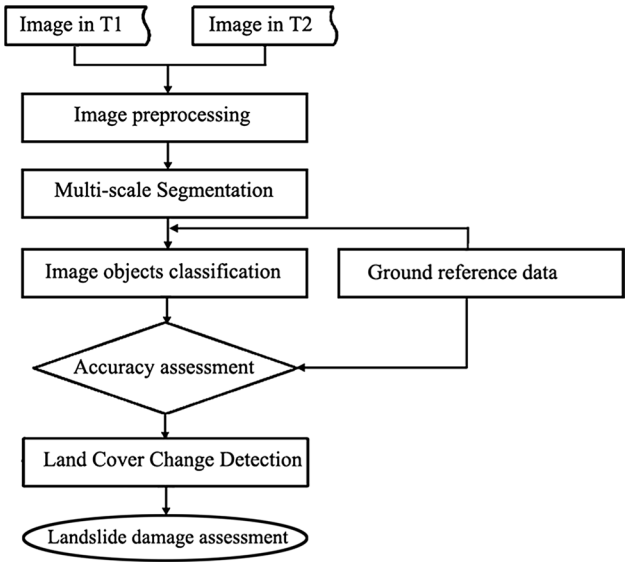

Fig. 9 Flow chart of the proposed OOCD approach

warp images. The second-order polynomial warping transformation was used as a geometric image correction model. Approximately 50 control points were used for each image to ensure accurate image registration. The root-mean-square errors (RMSE) of the 2002, 2010 and 2013 images were 1.81 pixels, 1.49 pixels and 1.67 pixels, respectively. The resolutions of the 2002, 2005 and 2013 images were matched with the 2005 QuickBird image resolution using a bilinear resampling interpolation method.

Object-based classification

Image segmentation

High-resolution images can be segmented into non-overlapping areas. Many types of segmentation algorithms exist, including the region growing approach (Xi et al. 2014), the genetic algorithm approach (Wang et al. 2009), the clustering-based approach (Demir and Ertürk 2009) and the multi-scale segmentation algorithm. The multi-scale segmentation algorithm can adequately describe a targeted object and the associated spatial semantic information (Zhang et al. 2014a). The multi-scale segmentation algorithm was proposed based on the principle of achieving the smallest amount of heterogeneity inside objects and the largest amount of heterogeneity between objects. The multi-scale segmentation algorithm is a bottom-up, region-merging technique that begins at the pixel level. Image objects are merged with larger image objects during each subsequent step. The merging process results in several successive object levels. Multi-scale segmentation has been utilised for various high-resolution image processing applications (Benz et al. 2004).

Multi-scale segmentation was used for high-resolution image segmentation in this study. Multi-scale segmentation and image classification are embedded within the eCognition Developer 8.7 software package. Resultant segmentations in eCognition Developer 8.7 are controlled by the scale, colour, compactness and shape parameters. The relationships among these parameters are described in Fig. 10.

The scale parameter is defined as the maximum standard deviation of the homogeneity in regard to the weighted image layers of the resulting image objects. Additionally, the scale parameter constrains the size of the image segment. Image objects can be obtained by modifying the scale parameter values. The higher the scale parameter value, the larger the resulting image objects. A "trial-and-error" method was used to determine the appropriate scale parameter values (Karydas and Gitas 2011). The scale value is gradually increased, and the segmentation results are distinguished via visual interpretation. The appropriate scale value is determined based on the agreement between the image objects acquired using multi-scale segmentation and actual geographic objects.

The homogeneity composition, which consists of colour and shape parameters, defines the total relative homogeneity for the resulting image objects. An appropriate homogeneity standard for resulting image objects is based on the agreement between the image object boundaries and actual geographic object boundaries. The "trial-and-error" method was also used to determine the appropriate compactness parameter values for each image.

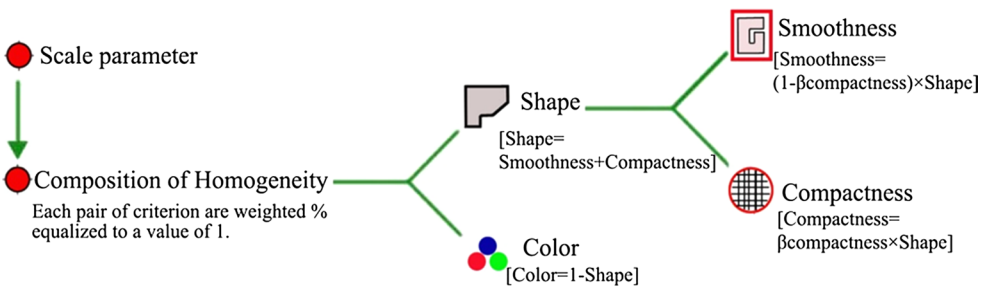

Fig. 10 Multi-scale conceptual flow chart based on the eCognition technical documentation

Image object classification using the 1-NN algorithm

Traditional image classification algorithms are mainly implemented using parametric models. Therefore, the image classification data or variables should fit a probability distribution, such as the Gaussian distribution (Jensen 2009). Few statistical models are able to accurately classify object-oriented land cover types due to random image object distributions. Therefore, object-oriented image classification is commonly performed using a nonparametric classifier. The simple nearest-neighbour (1-NN) algorithm is a highly effective classification model that is not based on a Gaussian distribution (Duda and Hart 1973). In the 1-NN algorithm, the image objects are classified by computing the Euclidean distance from the test objects to the nearest training sample objects.

The geometric, shape, spectral and textural parameters of the segmented image objects are used to classify the objects. These input variables are difficult to define using a statistical model. Therefore, the 1-NN algorithm is used to classify the segmented image objects in this study.

Change detection

Various change detection methods have been proposed using multi-temporal remote sensing images. According to Lu et al. (2004), change detection methods can be grouped into seven categories: algebra methods (Bindschadler et al. 2010), transformation methods (Celik 2009), the post-classification comparison approach (Ahlqvist 2008), advanced models (Tooke et al. 2009), geographic information system (GIS) approaches (Shalaby and Tateishi 2007) and visual analyses (Panigrahy et al. 2010). Among these change detection methods, the post-classification comparison approach possesses a relatively high level of accuracy. The post-classification comparison method can be used to obtain land cover change maps via comparing classified objects in different images.

The land cover maps in the study area were obtained using eCognition Developer 8.7. The final land cover maps were then imported into ArcGIS 10.0. The "intersect" function in ArcGIS 10.0 was used to automatically identify landslide deformation characteristics and create land cover change maps. Land cover change objects with areas less than 11 m^2 were ignored.

Experiments

Class definition

Field investigations and visual inspections of the original high-resolution images were used to divide the land cover types into five categories: bare land (B), building (Bu), road (R), water (W) and woodland (Wo). The change detection process in the study area aimed to extract land cover change information, i.e. whether or not changes occurred, and how the land changed. The dynamic land cover change was described using the format "land cover changed from classification A to classification B", e.g. "land cover changed from woodland to water".

The land cover change information was compiled by identifying the land cover change types, as listed in Table 2. The row labels represent land cover classification at C1, while the column labels represent land cover classification at C2. The format "land cover changed from classification C1 to C2" was abbreviated as "C1C2". For example, "BuW" represents a land cover classification change from building to woodland, while "NC" indicates that no change occurred.

Object-oriented classification

The object-oriented classification methods used in this study include both high-resolution image segmentation and the 1-NN classification algorithm.

Image segmentation

The trial-and-error method was used to select the appropriate scale parameters for image segmentation. The segmentation results will be fragmental if the scale parameter value is too small. However, the segmentations will be incomplete, and some small objects may not be recognised if the scale parameter is too large. Scale parameters of 20, 30, 40 and 50 were sequentially chosen. The scale parameter value of the first, coarsest level, which was originally created based on pixel units, was set to 20 for each image. However, the segmentation results showed that the image objects of the four images were fragmental. The scale value of the second level was then set to 30. In this case, the image object sizes mimicked the outlines of the original ground objects. In addition, the ground objects of the 2002, 2005 and 2010 images were completely segmented. The scale value of the third level was increased to 40. The results showed that this scale level was suitable for the 2013 image, while the ground objects were incompletely segmented for the 2002, 2005

Table 2 Land cover change types (rows are C1 and columns are C2)

Change types	Building	Woodland	Water	Bare land	Road
Building	NC	BuWo	BuW	BuB	BuR
Woodland	WoBu	NC	WoW	WoB	WoR
Water	WBu	WWo	NC	WB	WR
Bare land	BBu	BWo	BW	NC	BR
Road	RBu	RWo	RW	RB	NC

and 2010 images. The fourth level used a scale value of 50. The results of this analysis showed that the ground objects were incompletely segmented for all images. A portion of the 2002 IKONOS image was used as an example, as shown in Fig. 11. Figure 11 illustrates that a scale value of 30 is suitable for IKONOS image segmentation.

The multi-scale segmentation method is used only to determine an optimal segmentation scale for image objects classification, and the image objects under multi-scale segmentation levels are not classified in this study. One reason is that it is complex to classify the image objects under all the segmentation levels, because there are object inheritance, polymorphism and other features needed to be addressed in the classification process under multi-scale segmentation levels (Su et al. 2011). Another reason is that the classification accuracies of image objects under selected optimal segmentation scale are appropriate to the LCCD; it is not necessary to do image classification under multi-scale segmentation levels (Zhang et al. 2014b).

According to (Martha et al. 2011), the colour parameter is generally assigned a large weight, while the shape heterogeneity is assigned a small weight. The shape parameter is typically less than 0.3. The shape parameter was set to 0.2 for the four images in this study. The compactness values of the four images were set to 0.2, 0.5, 0.7 and 0.9. The test results show that a compactness parameter value of 0.7 provided a satisfactory segmentation result for all four images based on certain scale and shape parameters. The final segmentation results (Fig. 12) show that the ground objects were incompletely segmented for all four images.

Image object classification using the 1-NN algorithm

The scale parameter was set to 30 for the 2002, 2005 and 2010 images and 40 for the 2013 image. The image objects can be classified based on the selection of optimal image object features (Baatz and Schäpe 1999). The optimal object features were used as input variables for the 1-NN algorithm. The size of each high-resolution image is about 0.26 km^2; each high-resolution image is segmented into approximately 1300 image objects. The training samples of 1-NN algorithm are selected based on image objects, and these training samples are uniformly distributed throughout the study area. There are 5, 35, 35, 35 and 25 training samples used for the land cover types of road, water, building, woodland and bare land, respectively.

The optimal object features were mainly based on spectral attributes, layer values, geometry, position and texture attributes. A visual inspection method and a semi-automatic feature selection method in eCognition developer 8.7 were used to assess various combinations of the n-feature space. Among the analysed attributes, NDVI, A/P, brightness,

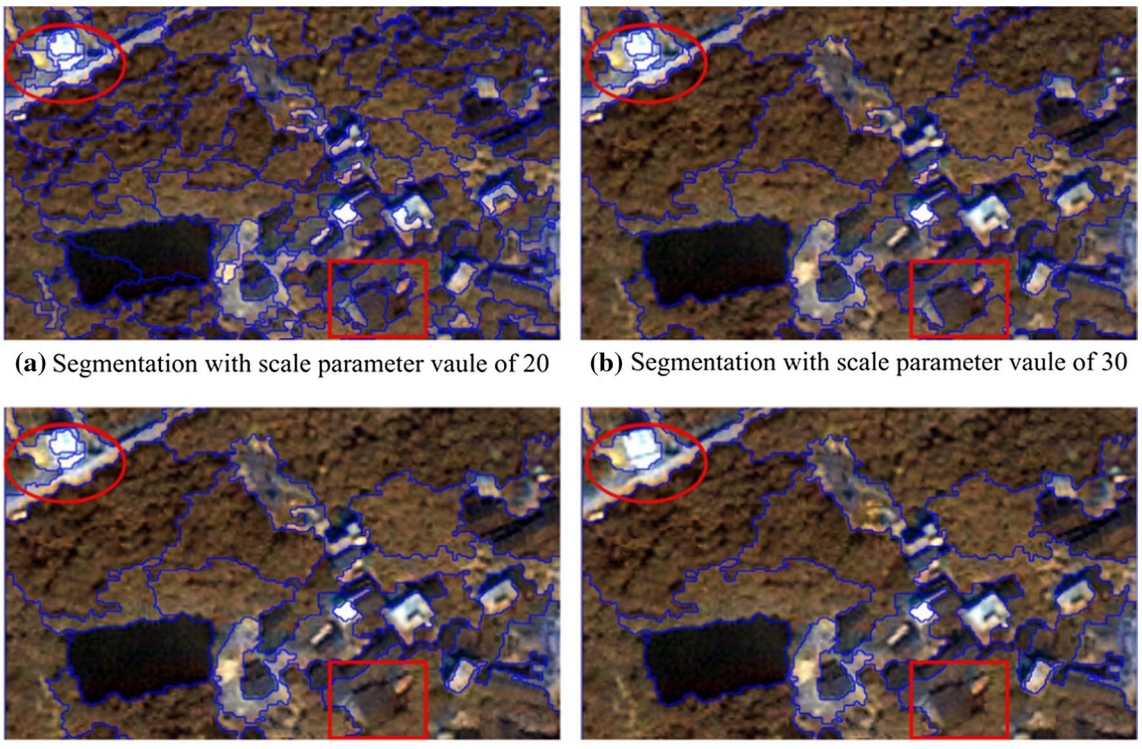

(a) Segmentation with scale parameter vaule of 20

(b) Segmentation with scale parameter vaule of 30

(c) Segmentation with scale parameter vaule of 40

(d) Segmentation with scale parameter vaule of 50

Fig. 11 Multi-scale segmentation with a shape value of 0.2, compactness value of 0.7 and various scale values

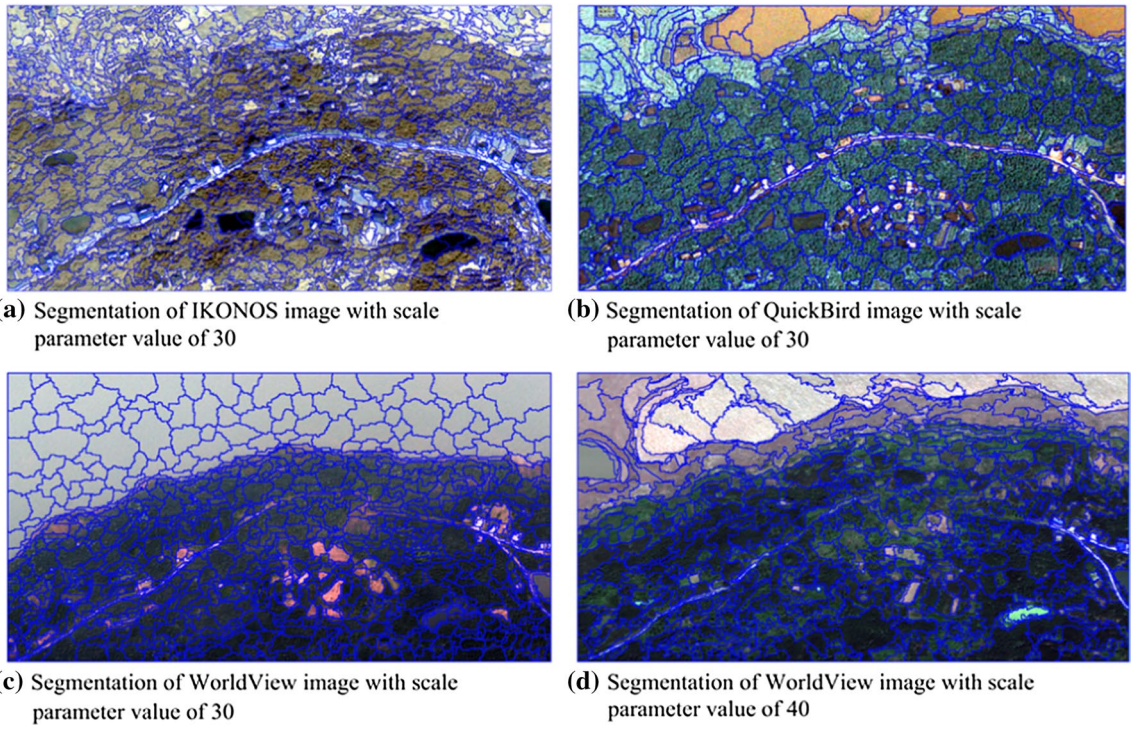

(a) Segmentation of IKONOS image with scale parameter value of 30

(b) Segmentation of QuickBird image with scale parameter value of 30

(c) Segmentation of WorldView image with scale parameter value of 30

(d) Segmentation of WorldView image with scale parameter value of 40

Fig. 12 Image object segmentation results with blue boundaries

Table 3 Descriptions of the object features

Object features	Description
NDVI	NDVI (normalised difference vegetation index) is mainly used for the detection of vegetation growth and coverage. It can be expressed as: NDVI = (p(nir) − p(red))/(p(nir) + p(red)), where p(red) and p(nir) represent the spectral reflectance measurements acquired in the visible (red) and near-infrared regions, respectively
A/P	A/P is an arithmetic feature that is defined as the perimeter-to-area ratio of a polygon. It expresses the shape feature of image objects. The higher the A/P value, the more compact the image objects
Brightness	Brightness expresses the strength of the image objects' light reflectance. Image objects with higher brightness values are able to reflect more light. For example, the road and building classes possess strong light reflectance abilities
GLCM entropy	GLCM (grey level co-occurrence matrix) entropy defines how often different combinations of pixel brightness values (grey levels) occur in an image. The GLCM is a common method that expresses the image texture features by studying the spatial correlation characteristics of grey scales
Standard deviation	Standard deviation measures the dispersion degree of pixel distributions in image objects. The smaller the standard deviation, the closer to the average value

GLCM entropy and the standard deviation (Table 3) were selected as input variables for the 1-NN algorithm. The IKONOS image does not contain the near-infrared band; therefore, those image objects do not contain the NDVI feature.

The final classification results are shown in Fig. 13 and Table 4. Figure 13 shows that the main land cover types on 9 September 2002 were woodland and bare land, encompassing areas of 163,648 and 75,986 m^2, respectively. The road in the study area covered an area of 6198 m^2. Seven ponds and numerous buildings were distributed on both sides of the road. Only one small body of water was observed, encompassing an area of 5083 m^2, because the water level of the TGR was 70 m. The main land cover type was woodland on 20 July 2005, encompassing an area of 192,775 m^2. Regions of bare land, buildings and water were also observed on both sides of the road, with areas of 32,530, 19,572 and 21,277 m^2, respectively.

The 8 October 2010 classification results show that woodland and water were the main land cover types, encompassing areas of 159,417 and 96,625 m^2, respectively. Few buildings and bare land regions were observed. Additionally, the

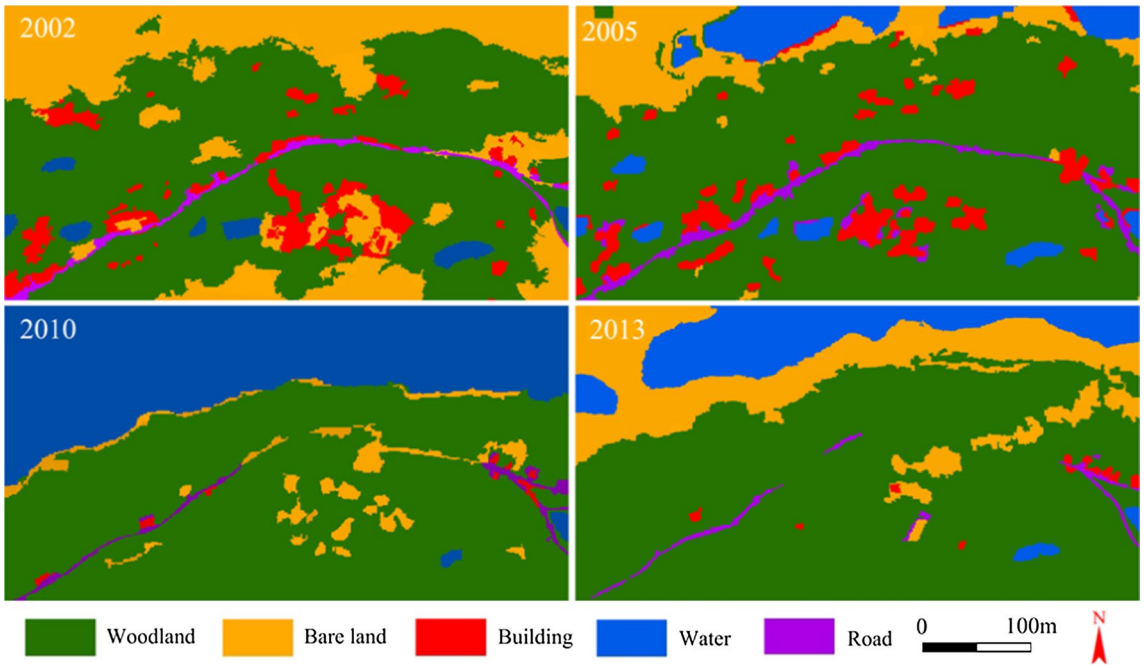

Fig. 13 Final object-based study area classification results using the 1-NN algorithm

Table 4 Areas of different land cover types from 2002 to 2013

Area (m^2)	Woodland	Bare land	Building	Water	Road
2002 Image	163,648	75,986	21,437	5083	6198
2005 Image	192,775	32,530	19,572	21,277	6198
2010 Image	159,417	11,053	2402	96,625	2855
2013 Image	178,931	52,213	2402	35,951	2855

roads became disconnected in the middle of the study area, covering an area of 2855 m^2. On 23 June 2013, the main land cover type was woodland, encompassing 178,931 m^2. Bare land and water were also present because the reservoir water level was 145 m. The road was intermittent, and fewer buildings were observed.

Classification accuracy assessment

Twenty-five per cent of the classification image objects from the 2002, 2005, 2010 and 2013 images were selected randomly to estimate the classification accuracy. The reference samples were confirmed through field investigations. In addition, the inaccessible image objects were identified via visual inspection, which was conducted based on field surveying and inspection of the geospatial imagery. Several accuracy evaluation indexes were used to assess the classification accuracy. Among these evaluation indexes, the Kappa Index of Agreement (KIA) is calculated based on the ratio of the model classification error to the error of a completely random classification (Stehman 1997). The KIA is based on a multivariate statistical analysis. The classification accuracy of the four images is listed in Table 5.

The IKONOS image from 2002 was found to have the lowest overall accuracy. This low accuracy was due to the 1 m resolution of the IKONOS image and lack of the NDVI feature. The overall accuracy of the 2010 Worldview-II image was the highest among the studied images. The woodland and water classifications had higher overall accuracy than the other land cover classes.

The 2013 land cover map was used to verify the accuracy of the object-oriented classification scheme based on field investigations. Figure 14a clearly illustrates a road in the south-western portion of the study area. Figure 14b shows a large piece of bare land meandering through the forest. The bare land was verified to be a large surface fissure. Figure 14c illustrates that the reservoir water, bare land and forest classes were distributed in the northern portion of the study area. Field surveys suggested that the land cover classification of the study area was satisfactory.

The object-oriented classification errors were mainly due to image quality, image segmentation and image object classification. In terms of image quality, the classification precision declined because of the topographic relief of the study area. The topographic relief results in the obvious changes of solar radiation, sky diffuse radiation and cross-radiation of adjacent image pixels. As a result, the phenomenon of the same object with different spectrums, and different spectrums with the

Table 5 Classification accuracy of image objects

Images	Accuracy	Woodland	Building	Water	Bare land	Road
2002	Producer's	0.906	0.726	0.903	0.879	0.725
	User's	0.736	0.939	0.897	0.967	0.942
	Total	Overall accuracy 0.862			KIA 0.807	
2005	Producer's	0.956	0.896	0.973	0.905	0.922
	User's	0.925	0.903	0.968	0.859	0.933
	Total	Overall accuracy 0.924			KIA 0.894	
2010	Producer's	0.986	0.895	1	0.898	0.935
	User's	0.982	0.907	0.961	0.926	0.926
	Total	Overall accuracy 0.942			KIA 0.912	
2013	Producer's	0.961	0.882	0.964	0.879	0.982
	User's	0.932	0.893	0.954	0.906	0.949
	Total	Overall accuracy 0.93			KIA 0.893	

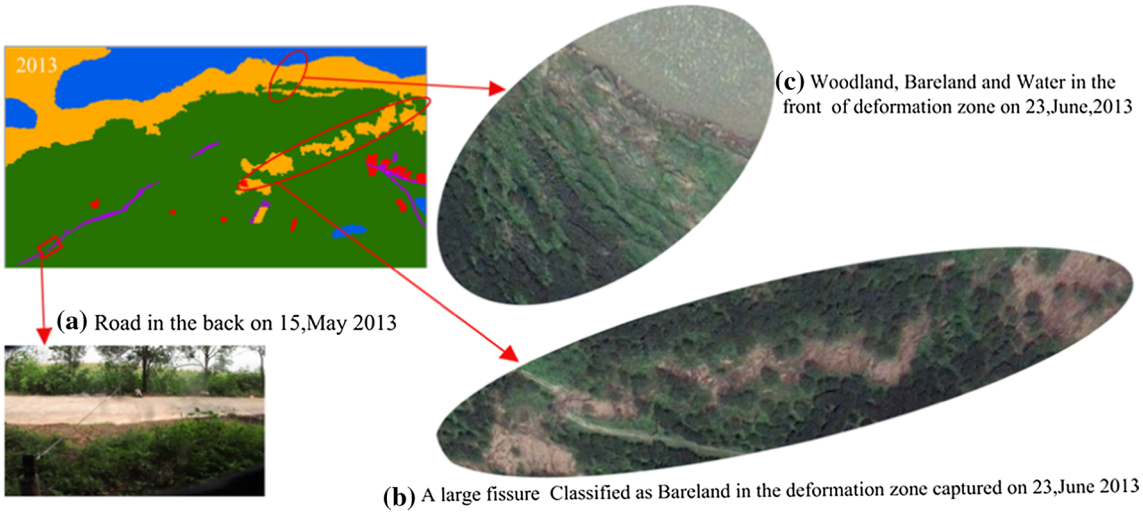

Fig. 14 Object-oriented classification verification using the 2013 land cover classification map based on field investigations

same object is caused, and the quality of remote sensing image processing and analysis declines (Lin et al. 2017; Zomer et al. 2002). In regard to image segmentation, the multi-scale segmentation algorithm identified the object boundaries by aggregating neighbouring pixels at the local spatial scale. The presence of mixed pixels around objects and terrain boundaries resulted in indeterminate categorisation areas. In addition, bare land boundaries have a high probability of being confused with water and woodland features.

Classification errors were generated because of spectral similarities between different classes. Based on the confusion matrix, the spectral characteristics of buildings had a high probability of being confused with the bare land and road classes. Therefore, the building and road classifications exhibit the lowest overall accuracy.

Results and discussion

Land cover change detection

The classification accuracy assessment demonstrated that land cover map comparisons can be used as the basis for LCCD. The final land cover change results are shown in Fig. 15 and Table 6.

Figure 15a and Table 6 show that the major land-use changes include from bare land to woodland and from bare land to water. The areas of change for BWo and BW were 31,457 and 16,194 m^2, respectively. These changes account for a combined 82% of all changes from 2002 to 2005. Figure 15a and Table 6 also show that the shifts from building to woodland and from building to bare land

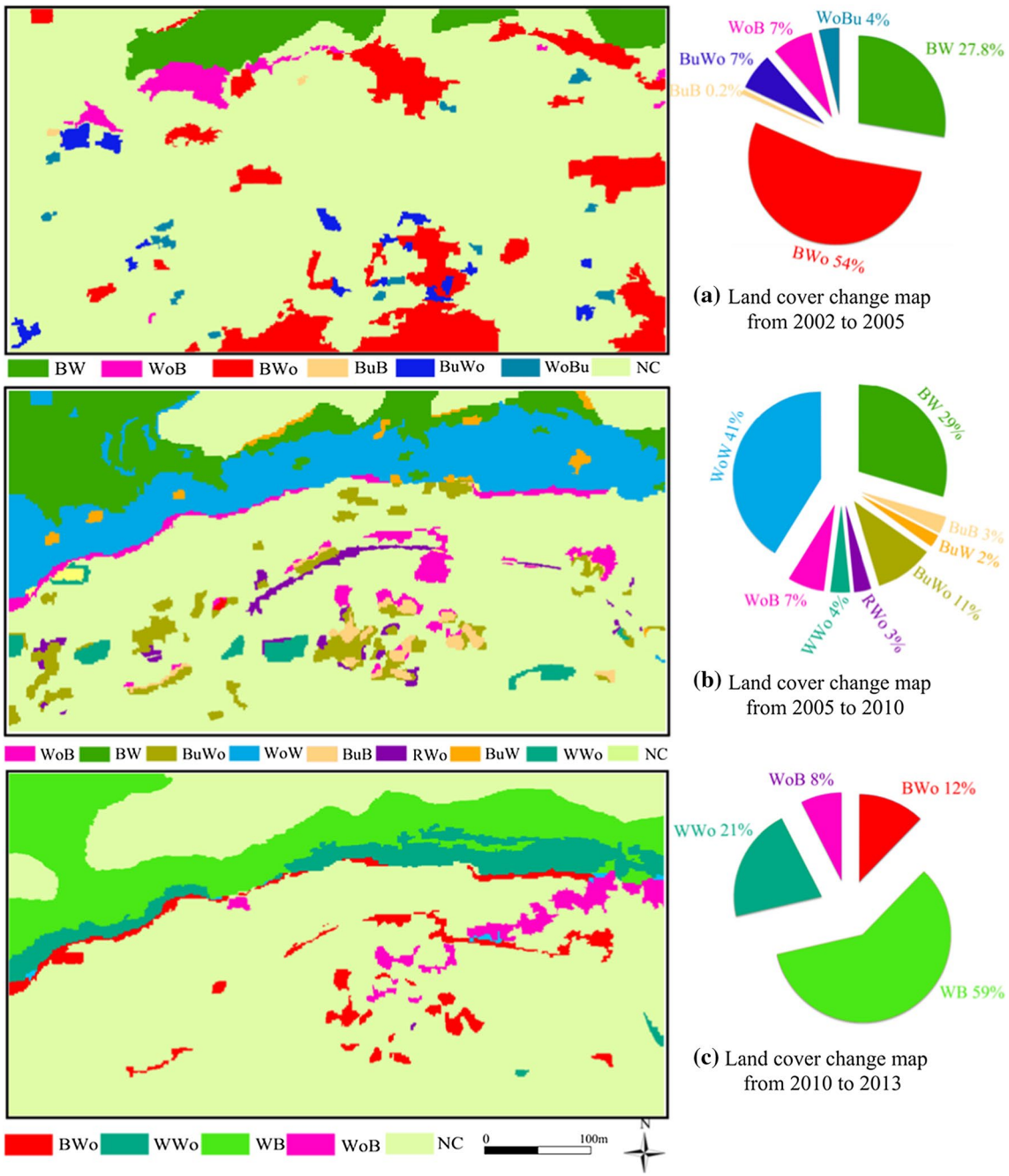

Fig. 15 Land cover change maps from 2002 to 2013 with land cover change pie charts, excluding "no-change" areas

Table 6 Areas of land cover change from September 2002 to June 2013

	Change types	BW	BWo	BuB	BuWo	WoB	WoBu	NC
2002–2005	Area (m^2)	16,194	31,457	117	4078	4078	2330	214,098
	Change types	BW	BuB	BuWo	BuW	WoB	WoW	RWo	WWo	NC
2005–2010	Area (m^2)	32,060	3309	11,543	2318	7274	44,832	3343	3862	163,812
	Change types	BWo	WoB	WWo	WB	NC				
2010–2013	Area (m^2)	9247	5674	15,941	44,733	196,756				

accounted for approximately 7% of the changed area. Specifically, buildings with a total area of 4195 m^2 were dismantled because they were located in a section of the study area that was destroyed. Meanwhile, 2330 m^2 of woodland was converted to building. This shift was due to a land shortage in the TGRA, which prompted the construction of various buildings in a relatively stable portion of the study area. Finally, 4078 m^2 of woodland in the northern portion of the study area was transformed to bare land.

Figure 15b and Table 6 illustrate that the dominant land cover changes from 2005 to 2010 included from woodland to water and from bare land to water, accounting for 70% of the total changes. The areas of change for WoW and BW were 44,832 and 32,060 m^2, respectively. Changes from building to woodland, from building to water and from building to bare land accounted for a combined total of approximately 16% of the changes. Buildings with a total area of 17,170 m^2 were dismantled. In addition, water to woodland conversions resulted in five ponds encompassing a total area of 3862 m^2 drying up. Additionally, 3343 m^2 of road was transformed to woodland.

The major land cover changes from 2010 to 2013 were from water to bare land and from water to woodland. These changes encompassed an area of 60,674 m^2, accounting for 80% of the total changes. The change from bare land to woodland accounted for approximately 12% of the total change, covering an area of 9247 m^2. In addition, change from woodland to bare land was observed along the road, encompassing a changed area of 5674 m^2.

Landslide damage assessment

The damage of the study area was assessed based on land cover change detection. The damages mainly occurred in the northern and central portions of the study area. The most serious damages occurred between 2005 and 2010. The main damage types included the submersion of woodland, destruction of buildings and roads, and formation of a large surface crack.

The results of "Land cover change detection" section showed that one of the main damage types was the submersion of woodland, covering approximately 28,891 m^2 from 2005 to 2010. The woodland included large areas of orange grove, pear trees and other economic trees. In addition, the woodland submersion reduced the incomes of local farmers. Approximately 21,365 m^2 of buildings in the study area were also destroyed, although 2330 m^2 of buildings were rebuilt. Most of the buildings were destroyed as a result of serious surface cracks and reservoir water submersion. Moreover, a 300-m road was seriously damaged from 2005 to 2010. The road was broken off in the middle part of the study area. Furthermore, 5674 m^2 of woodland became an interconnected area of bare land. This bare land area was verified to be a large surface crack that developed in the study area, as shown in Fig. 7d. However, it is difficult to identify the landslide surface cracks from the LCCD maps because the size of image object is larger than most of the surface cracks. Hence, the landslide deformation and surface cracks are identified and located mainly through field investigation. The field investigation is an important assistive tool for the LCCD to explore the landslide deformation characteristics under the micro-level.

Damage mechanism analysis of Tangjiao Landslide

Correlations between landslide groundwater levels and reservoir water level, seasonal rainfall

The groundwater levels of hydrology drills STK-1 on the frontal part, STK-2 on the middle part and STK-3 on the upper part of the study area from 10 August 2014 to 8 October 2015 are shown in Fig. 16. Meanwhile, the related reservoir water level and daily rainfall time series are also shown in Fig. 16. It can be seen from Fig. 16 that the groundwater levels of STK-1 were affected greatly by the fluctuation of reservoir water level. The groundwater level was high when the reservoir water level rose to 175 m from August 2014 to May 2015, while the groundwater level declined when the reservoir water level drawdown to 145 m from May 2015 to August 2015. The groundwater levels of STK-2 and STK-3 were affected weakly by the fluctuation of reservoir water level.

Meanwhile, Fig. 16 shows that the groundwater levels of all the hydrology drills were influenced greatly by the rainfall. For example, the groundwater levels of STK-2 and STK-3 rose gradually when the study area was in the rainy seasons from June 2015 to September 2015. In addition, some of the evidence suggested that the water-level fluctuation had greater influence on the groundwater level changes of STK-1 than the seasonal rainfall. For example, the groundwater levels of STK-1 declined gradually from June 2015 to September 2015 when the water level drawdown and the study area suffered seasonal heavy rainfall.

Correlations between LCCD and landslide groundwater levels

There are indirect correlations between landslide groundwater level changes and LCCD. Per the land cover change maps in Fig. 15a, b, the bare land and woodland classes in the northern portion of the study area were submerged due to a rising water level, which inducing a rise of groundwater level in the STK-1. Conversely, Fig. 15c illustrates that water accumulated in some bare land and woodland areas due to a dropping water level, which inducing a drawdown of the groundwater levels in the STK-1. These cyclic

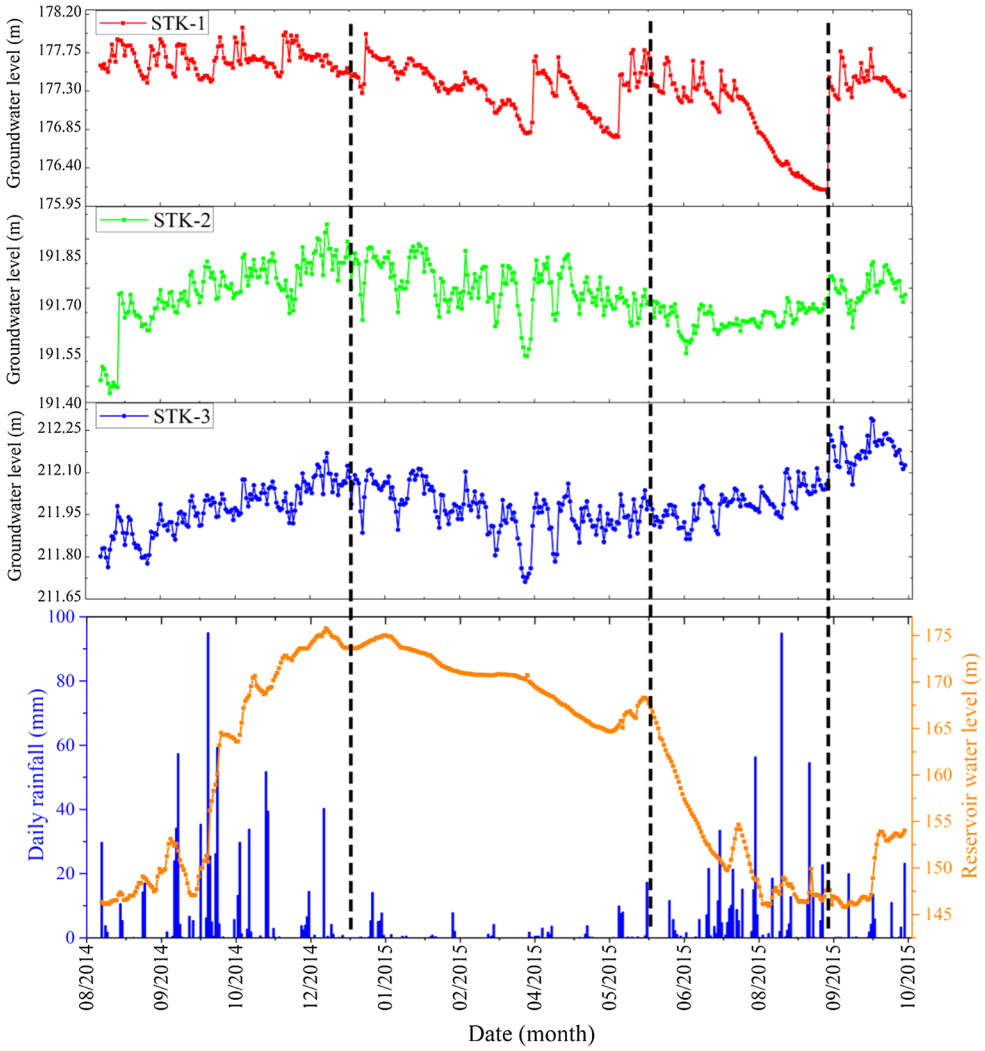

Fig. 16 Correlation curves between landslide groundwater levels and reservoir water level, seasonal rainfall

changes showed that the groundwater levels in the STK-1 rose and fall synchronously with the land cover changes of the study area. A literature review showed that landslide stability decreased when the groundwater levels declined, and landslide stability increased when the groundwater levels rose (Huang et al. 2017b; Zhang et al. 2012). Actually, there might be correlations between the changes of landslide stability and the changes of land cover in the study area.

Meanwhile, Fig. 15a, b also illustrates that many buildings were dismantled and transformed to other land cover types. In addition, Fig. 15b, c shows that the bare land area increased and a large crack appeared. The large crack illustrated the continuous deformation caused by landslides. The groundwater levels of the landslide may rose and drawdown more quickly than before if rainfall runoff and infiltration fill the crack, which inducing the rapid changes of the landslide stability. Hence, some attentions should be attracted to the relationships between land cover changes and groundwater level changes, to increase the landslide stability.

Damage mechanism analysis of Tangjiao Landslide

As discussed in "Natural geography of the Tangjiao Landslide" section, the reactivation of the Tangjiao Landslide was controlled by the geological conditions. The Tangjiao Landslide material was characterised by a medium permeability, loose structure and low mechanical strength. The freed surface was another passive factor for landslide deformation.

The results in "Land cover change detection" and "Landslide damage assessment" sections show that the main external causes of landslide damage were the reservoir water-level fluctuation and seasonal rainfall. The probable reason was that the rise of reservoir water level increased groundwater levels in the frontal part of the landside, while the drawdown of reservoir water level decreased groundwater levels in the frontal part. The decline of the groundwater level increased the reverse seepage pressure on the slide section of the landslide; as a result, the landslide deformation might increase. Seasonal rainfall also contributed to the landslide damage. The seasonal rainfall decreases the matric suction of the

rock-soil body and affects the slip zone. Additionally, the unit weight and seepage pressure of the slide body would continue to increase when rainfall filled the cracks inside the landslide.

Conclusion

This study proposes an OOCD approach for identifying damage characteristics in the study area of Tangjiao Landslide active block. The OOCD approach was applied to map land cover changes. The land-use classification results suggest that the object-oriented classification method produced accurate results for the high-resolution images. With the exception of the IKONOS image, these images elicited very high accuracy. A damage assessment was determined based on the land cover change maps. The main damage types included the submersion of woodland, damage to buildings and roads, and formation of a large surface crack. The geological conditions controlled the landslide instability, and the fluctuation of reservoir water level and seasonal rainfall were the key external factors triggering the instability of Tangjiao Landslide.

Acknowledgements This research was funded by the National Natural Sciences Foundation of China (No. 41572292).

References

Ahlqvist O (2008) Extending post-classification change detection using semantic similarity metrics to overcome class heterogeneity: a study of 1992 and 2001 us national land cover database changes. Remote Sens Environ 112(3):1226–1241

Baatz M, Schäpe A (1999) Object-oriented and multi-scale image analysis in semantic networks. In: Paper presented at the 2nd international symposium: operationalization of remote sensing

Benoit L, Briole P, Martin O, Thom C, Malet J-P, Ulrich P (2015) Monitoring landslide displacements with the geocube wireless network of low-cost gps. Eng Geol 195:111–121

Benz UC, Hofmann P, Willhauck G, Lingenfelder I, Heynen M (2004) Multi-resolution, object-oriented fuzzy analysis of remote sensing data for gis-ready information. ISPRS J Photogramm Remote Sens 58(3):239–258

Bindschadler RA, Scambos TA, Choi H, Haran TM (2010) Ice sheet change detection by satellite image differencing. Remote Sens Environ 114(7):1353–1362

Blaschke T, Hay GJ (2001) Object-oriented image analysis and scale-space: theory and methods for modeling and evaluating multi-scale landscape structure. Int Arch Photogramm Remote Sens 34(4):22–29

Blaschke T, Lang S, Lorup E, Strobl J, Zeil P (2000) Object-oriented image processing in an integrated gis/remote sensing environment and perspectives for environmental applications. Environ Inf Plan Politics Public 2:555–570

Carlotto MJ (2009) Effect of errors in ground truth on classification accuracy. Int J Remote Sens 30(18):4831–4849

Celik T (2009) Unsupervised change detection in satellite images using principal component analysis and-means clustering. IEEE Geosci Remote Sens Lett 6(4):772–776

Chen G, Hay GJ, Carvalho LM, Wulder MA (2012) Object-based change detection. Int J Remote Sens 33(14):4434–4457

Demir B, Ertürk S (2009) Clustering-based extraction of border training patterns for accurate svm classification of hyperspectral images. IEEE Geosci Remote Sens Lett 6(4):840–844

Dronova I, Gong P, Wang L (2011) Object-based analysis and change detection of major wetland cover types and their classification uncertainty during the low water period at poyang lake, china. Remote Sens Environ 115(12):3220–3236

Duda RO, Hart PE (1973) Pattern classification and scene analysis, vol 3. Wiley, New York

Duro DC, Franklin SE, Dubé MG (2012) A comparison of pixel-oriented and object-based image analysis with selected machine learning algorithms for the classification of agricultural landscapes using spot-5 hrg imagery. Remote Sens Environ 118:259–272

Elmqvist B, Ardö J, Olsson L (2008) Land use studies in drylands: an evaluation of object-oriented classification of very high resolution panchromatic imagery. Int J Remote Sens 29(24):7129–7140

Fiorucci F, Cardinali M, Carlà R, Rossi M, Mondini A, Santurri L, Ardizzone F, Guzzetti F (2011) Seasonal landslide mapping and estimation of landslide mobilization rates using aerial and satellite images. Geomorphology 129(1):59–70

Fourniadis I, Liu J, Mason P (2007) Landslide hazard assessment in the three gorges area, china, using aster imagery: Wushan–Badong. Geomorphology 84(1):126–144

Friedl MA, McIver DK, Hodges JC, Zhang X, Muchoney D, Strahler AH, Woodcock CE, Gopal S, Schneider A, Cooper A (2002) Global land cover mapping from MODIS: algorithms and early results. Remote Sens Environ 83(1):287–302

Gamanya R, De Maeyer P, De Dapper M (2009) Object-oriented change detection for the city of Harare, Zimbabwe. Expert Syst Appl 36(1):571–588

Gong P, Li X, Xu B (2006) Research issues with high-resolution image interpretation theory and application methods. Int J Remote Sens 10(1):1–5

Gusella L, Adams BJ, Bitelli G, Huyck CK, Mognol A (2005) Object-oriented image understanding and post-earthquake damage assessment for the 2003 Bam, Iran, earthquake. Earthq Spectra 21(S1):225–238

Huang F, Yin K, Tao H, Chao Z, Jun Z (2016a) Influencing factor analysis and displacement prediction in reservoir landslides—a case study of three gorges reservoir (China). Tehnički vjesnik 23(2):617–626

Huang F, Yin K, Zhang G, Gui L, Yang B, Liu L (2016b) Landslide displacement prediction using discrete wavelet transform and extreme learning machine based on chaos theory. Environ Earth Sci 75(20):1376

Huang F, Huang J, Jiang S, Zhou C (2017a) Landslide displacement prediction based on multivariate chaotic model and extreme learning machine. Eng Geol 218:173–186

Huang F, Luo X, Liu W (2017b) Stability analysis of hydrodynamic pressure landslides with different permeability coefficients affected by reservoir water level fluctuations and rainstorms. Water 9(7):450

Huang F, Yin K, Huang J, Gui L, Wang P (2017c) Landslide susceptibility mapping based on self-organizing-map network and extreme learning machine. Eng Geol 223:11–22

Jensen JR (2009) Remote sensing of the environment: an earth resource perspective 2/e. New Delhi, Pearson Education India

Karydas CG, Gitas IZ (2011) Development of an IKONOS image classification rule-set for multi-scale mapping of mediterranean rural landscapes. Int J Remote Sens 32(24):9261–9277

Kirschbaum DB, Fukuoka H (2012) Remote sensing and modeling of landslides: detection, monitoring and risk evaluation. Environ Earth Sci 66(6):1583

Kumar SV, Peters-Lidard CD, Tian Y, Houser PR, Geiger J, Olden S, Lighty L, Eastman JL, Doty B, Dirmeyer P (2006) Land information system: an interoperable framework for high resolution land surface modeling. Environ Model Softw 21(10):1402–1415

Lan H, Zhou C, Wang L, Zhang H, Li R (2004) Landslide hazard spatial analysis and prediction using gis in the Xiaojiang watershed, Yunnan, China. Eng Geol 76(1):109–128

Laura DR, King DJ (2011) Comparison of pixel-and object-based classification in land cover change mapping. Int J Remote Sens 32(6):1505–1529

Lin Q, Huang H, Chen L, Chen E (2017) Topographic correction method for steep mountain terrain images. J Remote Sens 21(5):776–784

Lu D, Mausel P, Brondizio E, Moran E (2004) Change detection techniques. Int J Remote Sens 25(12):2365–2401

Mallinis G, Koutsias N, Tsakiri-Strati M, Karteris M (2008) Object-based classification using Quickbird imagery for delineating forest vegetation polygons in a mediterranean test site. ISPRS J Photogramm Remote Sens 63(2):237–250

Martha TR, Kerle N, Van Westen CJ, Jetten V, Kumar KV (2011) Segment optimization and data-driven thresholding for knowledge-based landslide detection by object-based image analysis. IEEE Trans Geosci Remote Sens 49(12):4928–4943

Mas J-F (1999) Monitoring land-cover changes: a comparison of change detection techniques. Int J Remote Sens 20(1):139–152

Mathieu R, Aryal J (2007) Object-based classification of ikonos imagery for mapping large-scale vegetation communities in urban areas. Sensors 7(11):2860–2880

Metternicht G, Hurni L, Gogu R (2005) Remote sensing of landslides: an analysis of the potential contribution to geo-spatial systems for hazard assessment in mountainous environments. Remote Sens Environ 98(2):284–303

Pacifici F, Chini M, Emery WJ (2009) A neural network approach using multi-scale textural metrics from very high-resolution panchromatic imagery for urban land-use classification. Remote Sens Environ 113(6):1276–1292

Panigrahy RK, Kale MP, Dutta U, Mishra A, Banerjee B, Singh S (2010) Forest cover change detection of Western Ghats of Maharashtra using satellite remote sensing based visual interpretation technique. Curr Sci 98(5):657–664

Platt RV, Rapoza L (2008) An evaluation of an object-oriented paradigm for land use/land cover classification*. Prof Geogr 60(1):87–100

Qin Y, Niu Z, Chen F, Li B, Ban Y (2013) Object-based land cover change detection for cross-sensor images. Int J Remote Sens 34(19):6723–6737

Shalaby A, Tateishi R (2007) Remote sensing and GIS for mapping and monitoring land cover and land-use changes in the Northwestern coastal zone of Egypt. Appl Geogr 27(1):28–41

Song K, Yan E, Zhang G, Lu S, Yi Q (2015) Effect of hydraulic properties of soil and fluctuation velocity of reservoir water on landslide stability. Environ Earth Sci 74(6):5319–5329

Stehman SV (1997) Selecting and interpreting measures of thematic classification accuracy. Remote Sens Environ 62(1):77–89

Su X, Wu W, Li H, Han Y (2011) Land-use and land-cover change detection based on object-oriented theory. In: Paper presented at the international symposium on image and data fusion

Tong X, Hong Z, Liu S, Zhang X, Xie H, Li Z, Yang S, Wang W, Bao F (2012) Building-damage detection using pre- and post-seismic high-resolution satellite stereo imagery: a case study of the May 2008 Wenchuan earthquake. ISPRS J Photogramm Remote Sens 68:13–27

Tooke TR, Coops NC, Goodwin NR, Voogt JA (2009) Extracting urban vegetation characteristics using spectral mixture analysis and decision tree classifications. Remote Sens Environ 113(2):398–407

Van Westen C, Getahun FL (2003) Analyzing the evolution of the Tessina landslide using aerial photographs and digital elevation models. Geomorphology 54(1):77–89

Vijay R, Kushwaha VK, Chaudhury AS, Naik K, Gupta I, Kumar R, Wate SR (2016) Assessment of tourism impact on land use/land cover and natural slope in Manali, India: a geospatial analysis. Environ Earth Sci 75(1):20

Walker J, Blaschke T (2008) Object-based land-cover classification for the phoenix metropolitan area: optimization versus transportability. Int J Remote Sens 29(7):2021–2040

Walter V (2004) Object-based classification of remote sensing data for change detection. ISPRS J Photogramm Remote Sens 58(3):225–238

Wang J, Tang J, Liu J, Ren C, Liu X, Feng J (2009) Alternative fuzzy cluster segmentation of remote sensing images based on adaptive genetic algorithm. Chin Geogr Sci 19(1):83–88

Wasowski J, Bovenga F (2014) Investigating landslides and unstable slopes with satellite multi temporal interferometry: current issues and future perspectives. Eng Geol 174:103–138

Xi T, Schreurs R, Heerink WJ, Bergé SJ, Maal TJ (2014) A novel region-growing based semi-automatic segmentation protocol for three-dimensional condylar reconstruction using cone beam computed tomography (cbct). PLoS ONE 9(11):e111126

Zhang M, Dong Y, Sun P (2012) Impact of reservoir impoundment-caused groundwater level changes on regional slope stability: a case study in the Loess Plateau of Western China. Environ Earth Sci 66(6):1715–1725

Zhang L, Jia K, Li X, Yuan Q, Zhao X (2014a) Multi-scale segmentation approach for object-based land-cover classification using high-resolution imagery. Remote Sens Lett 5(1):73–82

Zhang ZJ, Li AN, Lei GB, Bian JH, Wu BF (2014b) Change detection of remote sensing images based on multi-scale segmentation and decision tree algorithm over mountainous area: a case study in Panxi region, Sichuan province. Acta Ecol Sin 34(24):7222–7232

Zomer R, Ustin S, Ives J (2002) Using satellite remote sensing for DEM extraction in complex mountainous terrain: landscape analysis of the Makalu Barun National Park of eastern Nepal. Int J Remote Sens 23(1):125–143